

NOSE-RADIUS INFLUENCE ON DRAG AND LIFT OF ROUND LEADING EDGES IN HYPERSONIC AIRFLOW

Wilson F. N. Santos

National Institute for Space Research
Combustion and Propulsion Laboratory
12630-000 Cachoeira Paulista, SP, Brazil
wilson@lcp.inpe.br

Abstract. *In order to investigate the aerodynamic performance of round leading edges, a series of numerical simulations by parametrically changing the nose radius and the angle of attack was conducted. Twenty combinations of nose radius and angle of attack were used in the simulation. The computational investigation was performed in a rarefied hypersonic flow by using the Direct Simulation Monte Carlo (DSMC) method. The DSMC calculations examined drag coefficient, lift coefficient and lift-to-drag ratio to changes not only on the angle of attack but also on the nose radius of the leading edges. Comparisons based on drag, lift and lift-to-drag ratio are made between these round leading edges and sharply pointed leading edges. For the flow conditions considered, the analysis showed that significant differences between sharp, aerodynamically sharp and blunt leading edges were noted on the aerodynamic surface properties. It was found that the lift coefficient decreased by increasing the nose radius of the leading edges. It was inferred from the analysis that a tradeoff between performance, lift-to-drag ratio, and aerodynamic heating, heat flux, is required for an optimal hypersonic vehicle design, since the heat flux is inversely proportional to the nose radius of the leading edge.*

Keywords: *Hypersonic Flow, Rarefied Flow, DSMC, Round Leading Edge, Angle-of-attack.*

1. INTRODUCTION

An efficient design of future airbreathing hypersonic vehicle will depend on high-lift low-drag configurations in order to overcome the aerodynamic forces involved in high-speed flight. In this fashion, a waverider, pioneered by Nonweiler (1959), has been considered as one of the promising vehicle concepts under consideration. A waverider is a lifting body which is derived from a known analytical flowfield such as flow over a two-dimensional wedge or flow around a slender cone. Waveriders are vehicles designed so that the bow shock is everywhere attached to the sharp leading edge. The sharp-leading edges of waverider configurations are a dominant factor in their high lift-to-drag (L/D) ratio compared to conventional aerospace designs.

Usually, it is extremely difficult to construct a perfectly sharp leading edge. Any manufacturing error results in a significant deviation from the design contour. Even with the most efficient and careful fabrication process, the leading edges will be several microns thick. Moreover, sharp edges are difficult to maintain because they are easily damaged. It is not only due to difficulties in manufacturing technology and in the strength of the material that ideally sharp leading edges on airframes are impossible to achieve in practice. In addition to either handling or manufacturing requirements pointed, actual flight vehicle will include some degree of bluntness dictated by heating requirements. This is especially important given that heating rate on rounded edges (circular cylinder) scales inversely with the square root of the stagnation-point radius. Nevertheless, shock detachment distance on a cylinder, with associated leakage, scales with the radius of curvature. In this scenario, shock wave will be detached from the leading edge and, hence, the aerodynamic performance — L/D ratio — of the vehicle may be degraded from ideal performance, since the high-pressure gas from the lower surface may communicate with the gas on the upper surface. Therefore, there is an unavoidable compromise between aerodynamic performance and heating survivability. As a result, designing a hypersonic vehicle leading edge involves a tradeoff between making the leading edge sharp enough to obtain acceptable aerodynamic and propulsion efficiency and blunt enough to reduce the aerodynamic heating in the stagnation region.

Based on stagnation point heating and total drag, the overall performance of round shapes were compared to non-circular shapes in Santos (2004). The analysis showed that round leading edges provide smaller stagnation point heating and larger total drag coefficient than flat-faced leading edges. In Santos (2005a, 2005b and 2007), a parametric study was performed on round leading edges with a great deal of emphasis placed on the gas-surface interaction effects. Incomplete surface accommodation effects in rarefied gas flow were studied by using the Direct Simulation Monte Carlo (DSMC) method in conjunction with the Cercignani-Lampis-Lord gas surface interaction model. It was found from the investigation that it becomes imperative to take surface accommodation into account in order to make accurate predictions of the aerodynamic forces on, and heat transfer rates to, bodies in rarefied hypersonic flow.

In the present account effort is directed toward examining computationally the influence of the angle of attack and the nose radius on the aerodynamic surface quantities. The knowledge of the aerodynamic surface properties at zero angle of attack (Santos, 2004, 2005a, 2005b, and 2007) is not sufficient to predict with certainty the flow characteristics over these shapes with incidence. Of particular interest in this analysis is the aerodynamic performance of the leading

edges since blunt leading edges at incidence will allow leakage of the high-pressure from lower surface into the upper surface region, causing a reduction in the lift.

The study at hand computes the flow around various combinations of nose radius and angle of attack, covering from sharp to blunt leading edges. The essential characteristics of the angle of attack impact on heat transfer, drag, lift and L/D ratio will be examined for positive angle of attack with 5, 10, 15 and 20 degrees of incidence. Attention is focused on the low-density region in the upper atmosphere. For the transitional hypersonic flow, at high Mach number and high altitude, the flow departs from thermal equilibrium and the energy exchange into the various modes due to the vibrational excitation and relaxation becomes important. For the high altitude/high Knudsen number of interest, the flowfield is sufficient rarefied that continuum method is inappropriate. Alternatively, DSMC method will be employed to calculate the rarefied hypersonic two-dimensional flow on the round leading-edges.

2. LEADING EDGE GEOMETRY DEFINITION

The round leading edges are modeled by assuming a sharp-edged wedge of half angle θ with a reference circular cylinder of radius R inscribed tangent to the wedge. The round leading edges are inscribed between the wedge and the cylinder. The circular cylinder diameter provides a reference for the amount of blunting desired on the leading edges. It was assumed a wedge half angle of 10 degrees and a reference circular cylinder diameter of 10^{-2} m. In addition to the reference circular cylinder, four more circular cylinders with different nose radii were chosen for round leading edges. The dimensionless nose radius R_N/λ_∞ for the four bodies are 0.02, 0.1, 1.0 and 2.0, where λ_∞ is the freestream mean free path. Figure 1(a) illustrates the construction for the round leading edges investigated.

It was assumed that the leading edges are infinitely long but only the length L is considered, since the wake region behind the leading edges is not of interest in this investigation.

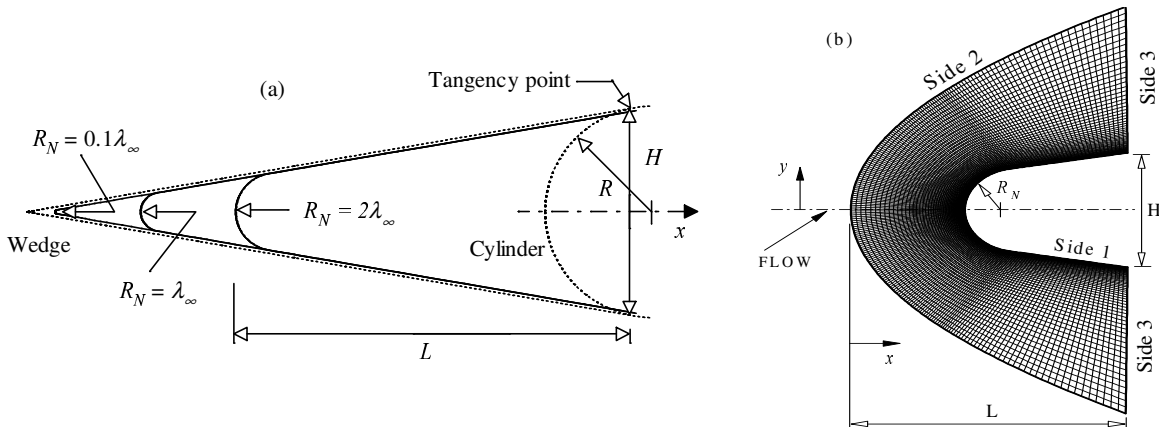


Figure 1: Drawing illustrating (a) the leading edge shapes and (b) the computational domain.

3. COMPUTATIONAL METHOD AND PROCEDURE

The Direct Simulation Monte Carlo (DSMC) method (Bird, 1994) has been very effective as an engineering tool for the prediction of rarefied flow. The DSMC method employs thousands simulator particles in order to reproduce the behavior of a far larger number of real atoms or molecules with the flow. The simulator particles are allowed to move and collide, while the computer stores their position coordinates, velocities and other physical properties such as internal energy. The velocity and position of simulated molecules are allowed to change with and through the boundaries of a fixed number of cells in a discretized computation space as time is advance. The post collision velocity of interacting molecules is determined in a probabilistic manner. After many time steps, average macroscopic gas properties of the simulated molecules in each cell produce a flow solution within the boundaries of the domain.

In the present study, molecular collisions are modeled by the variable hard sphere (VHS) molecular model (Bird, 1981) and by the no time counter (NTC) collision sampling technique (Bird, 1989). The mechanics of the energy exchange processes between kinetic and internal modes for rotation and vibration are controlled by the Borgnakke-Larsen statistical model (Borgnakke and Larsen, 1975). Simulations are performed using a non-reacting gas model consisting of two chemical species, N_2 and O_2 . All collisions exchange translational energy, with one in 5 exchanged rotational energy and one in 50 exchanged vibrational energy.

In order to implement the particle-particle collisions, a grid is superimposed on the computational region of interest. In such a context, the flowfield is divided into an arbitrary number of regions, which are subdivided into computational cells. The cells are further subdivided into four subcells, two subcells/cell in each direction. The cell provides a convenient reference sampling of the macroscopic gas properties, whereas the collision partners are selected from the

same subcell for the establishment of the collision rate.

The computational domain used for the calculation is made large enough so that body disturbances do not reach the upstream and side boundaries, where freestream conditions are specified. A schematic view of the cell layout is depicted in Fig. 1(b). The simulation of rarefied flows using DSMC method requires boundary conditions to be specified at all inflow and outflow boundaries. Inflow boundary conditions are usually determined by the flow under investigation. Outflow boundary conditions are generally not known a priori and certain assumptions are necessary. In this way, side 1 is defined by the body surface. Diffuse reflection with complete surface thermal accommodation is the condition applied to this side. Side 2 is the freestream side through which simulated molecules enter and exit. Finally, the flow at the downstream outflow boundary, side 3, is predominantly supersonic and vacuum condition is specified (Bird, 1994). For hypersonic flow, a vacuum boundary condition is suitable since the flow velocities are generally high enough to prevent a significant number of particles from entering the flowfield at such boundary.

The freestream and flow conditions used in the present calculations are those given by Santos (2005a) and summarized in Tab. 1 and Tab. 2, respectively. The freestream velocity V_∞ , assumed to be constant at 3.56 km/s, corresponds to freestream Mach number M_∞ of 12. The leading edge surface has a constant temperature T_w of 880 K for all cases considered.

Table 1: Freestream Conditions

Temperature T_∞ (K)	Pressure p_∞ (N/m ²)	Density ρ_∞ (kg/m ³)	Number density n_∞ (m ⁻³)	Viscosity μ_∞ (Ns/m ²)	Mean free path λ_∞ (m)	Velocity V_∞ (m/s)
220.0	5.582	8.753×10^{-5}	1.8209×10^{21}	1.455×10^{-5}	9.03×10^{-4}	3560

Table 2: Gas Properties

	Mole fraction X	Molecular mass m (kg)	Molecular diameter d (m)	Viscosity index ω
O ₂	0.237	5.312×10^{-26}	4.01×10^{-10}	0.77
N ₂	0.763	4.65×10^{-26}	4.11×10^{-10}	0.74

By assuming the nose diameter as the characteristic length, the overall Knudsen number Kn_D corresponds to 25, 5, 0.5, and 0.25 for nose radius R_N/λ_∞ of 0.02, 0.1, 1.0, and 2.0, respectively. The Reynolds number per unit of meter is $Re_\infty = 21416.3$, also based on conditions in the undisturbed stream.

In order to simulate the angle-of-attack impact on the aerodynamic surface quantities, the DSMC calculations were performed independently for five distinct numerical values of α , i.e., 0, 5, 10, 15 and 20 degrees.

4. COMPUTATIONAL RESULTS AND DISCUSSION

This section focuses on the effects that take place on the aerodynamic surface quantities due to changes on the angle of attack as well as on the nose radius. Aerodynamic surface quantities of particular interest in the transitional flow regime are number flux, heat transfer, wall pressure, wall shear stress, drag and lift. In this scenario, this section will discuss and compare differences of these quantities expressed in dimensionless coefficient form.

4.1. Number Flux

The number flux N is calculated by sampling the molecules impinging on the surface by unit time and unit area. A flux is regarded as positive if it is directed toward the body surface. The effect on number flux due to variations on the angle of attack α is illustrated in Figs. 2 and 3 for round leading edges with R_N/λ_∞ of 0.02 and 2.0, which correspond to the sharpest and the bluntest leading edge, respectively. In this set of diagrams, the dimensionless number flux N_f stands for the number flux N normalized by $n_\infty V_\infty$, where n_∞ is the freestream number density and V_∞ is the freestream velocity. In addition, the dimensionless arc length S is the arc length s along the body surface, measured from the stagnation point, normalized by the freestream mean free path λ_∞ . The number flux distributions for R_N/λ_∞ of 0.1 and 1.0 are intermediate to those presented in Figs. 2 and 3 and, therefore, they will not be shown.

Looking first at Figs. 2(a) and 2(b), which correspond, respectively, to the number flux distributions on the windward and leeward sides of the body surface, it is observed that the number flux presents the maximum value at the vicinity of the stagnation region along the cylindrical portion of the leading edges and drops off sharply up to the cylindrical-portion/afterbody junction for the angle of attack range investigated. In contrast, by comparing to the zero-degree angle of attack case, the number flux decreases along the leeward side, due to the flow expansion, and it increases along the windward side of the leading edge, due to the flow compression. This is an expected behavior for

positive angle of attack. Also, it may be recognized from this set of figures that the pick value for the number flux, initially at the stagnation point for zero-degree angle of attack, slightly increases and moves to the windward side of the body surface.

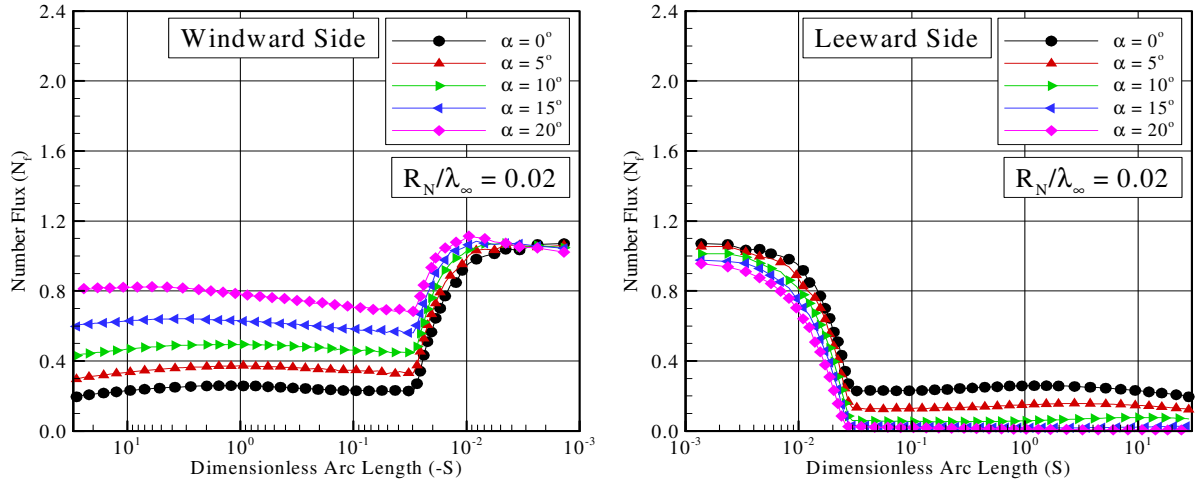


Figure 2: Distributions of the dimensionless number flux N_f along the (a) windward side and (b) leeward side as a function of the angle of attack for round leading edge with R_N/λ_∞ of 0.02.

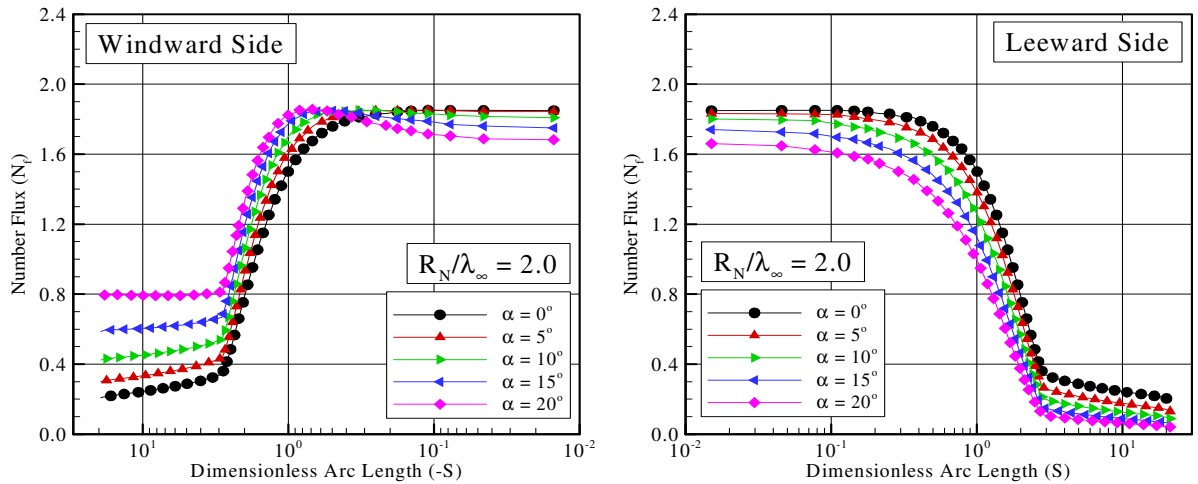


Figure 3: Distributions of the dimensionless number flux N_f along the (a) windward side and (b) leeward side as a function of the angle of attack for round leading edge with R_N/λ_∞ of 2.0.

Turning next to Figs. 3(a) and 3(b), for the zero-degree angle of incidence, it is noted that the number flux presents approximately a constant high value along the first half of the cylindrically portion of the leading edge, and then decreases significantly up to the cylindrically-portion/afterbody junction. After that, the number flux N_f still decreases along the afterbody surface, in contrast to the $R_N/\lambda_\infty = 0.02$ case. This set of figures reveals clearly that the number flux to the leading edge relies on the nose radius in that it increases with increasing the leading-edge nose radius. This enhancement in the number flux is related to the collisions of two groups of molecules; the molecules reflecting from the nose region of the leading edge and the molecules oncoming from the freestream. The molecules that are reflected from the body surface, which have a lower kinetic energy interact with the oncoming freestream molecules, which have a higher kinetic energy. Thus, the surface-reflected molecules re-collide with the body surface, which produce an increase in the dimensionless number flux in this region. At positive angle of attack, the stagnation point moves to the windward side of the leading edges. Consequently, the number flux dramatically increases along the windward side and decreases along the leeward side, due to the flow compression and flow expansion around the leading edges.

4.2. Heat Transfer Coefficient

The heat transfer coefficient C_h is defined as being,

$$C_h = \frac{q_w}{\frac{1}{2}\rho_\infty V_\infty^3} \quad (1)$$

where q_w is the net heat flux to the body surface and ρ_∞ is the freestream density.

The heat flux q_w to the body surface is calculated by the net energy flux of the molecules impinging on the surface. The net heat flux q_w is related to the sum of the translational, rotational and vibrational energies of both incident and reflected molecules as defined by,

$$q_w = q_i + q_r = \sum_{j=1}^N \left\{ \left[\frac{1}{2} m_j v_j^2 + e_{Rj} + e_{Vj} \right]_i + \left[\frac{1}{2} m_j v_j^2 + e_{Rj} + e_{Vj} \right]_r \right\} \quad (2)$$

where N is the number of molecules colliding with the surface by unit time and unit area, m is the mass of the molecules, v is the velocity of the molecules, e_R and e_V stand for the rotational and vibrational energies, respectively. Subscripts i and r refer to incident and reflected molecules.

The impact of the angle-of-attack on the heat transfer coefficient C_h is illustrated in Figs. 4 and 5 for round leading edges with R_N/λ_∞ of 0.02 and 2.0, respectively. It is clearly noticed from these plots that the heat transfer coefficient C_h is sensitive not only to the nose radius R_N but also to the angle of attack α .

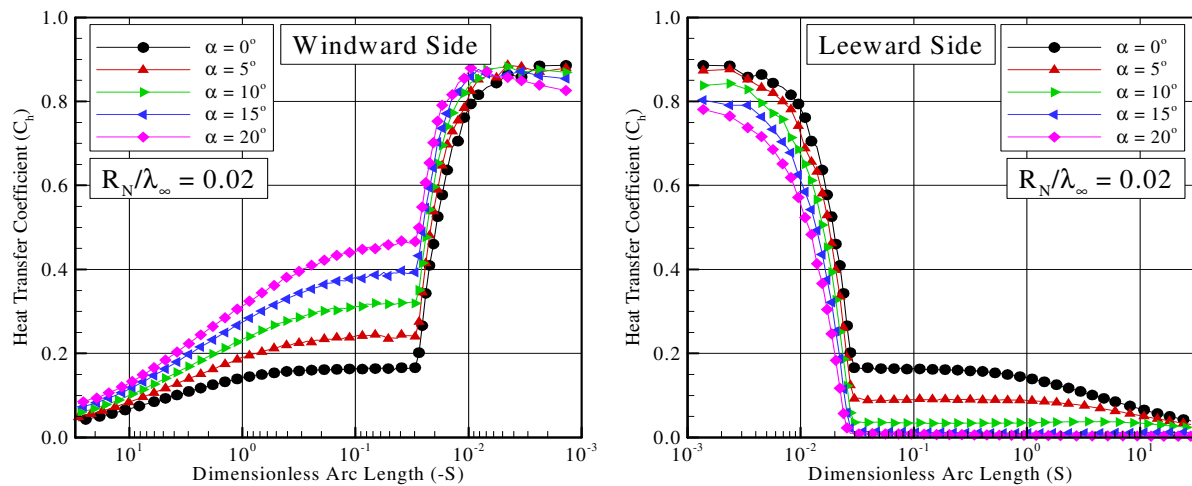


Figure 4: Distributions of heat transfer coefficient C_h along the (a) windward side and (b) leeward side as a function of the angle of attack for round leading edge with R_N/λ_∞ of 0.02.

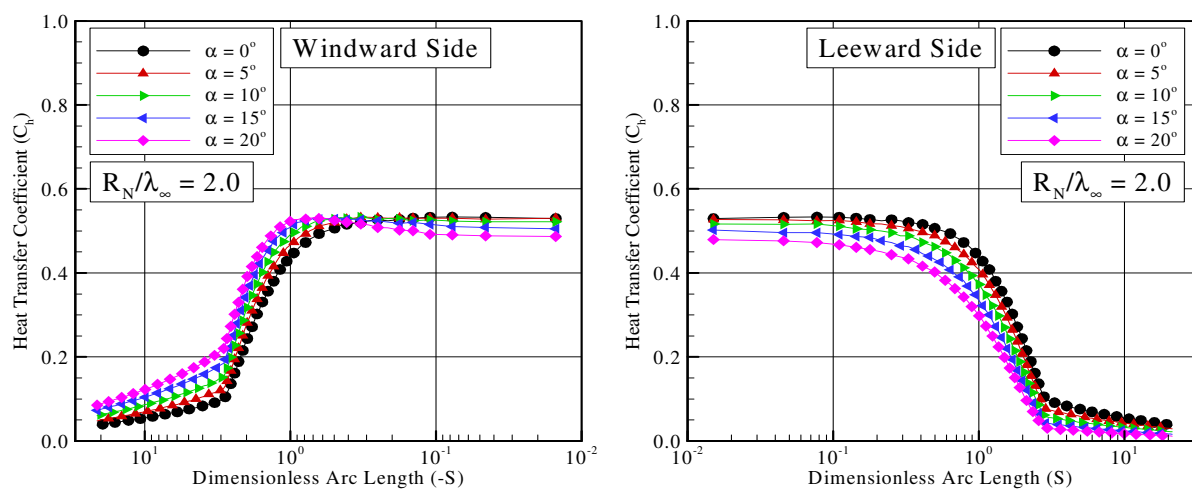


Figure 5: Distributions of heat transfer coefficient C_h along the (a) windward side and (b) leeward side as a function of the angle of attack for round leading edge with R_N/λ_∞ of 2.0.

In general, the heat transfer coefficient C_h presents the maximum value at the stagnation region and drops off sharply along the cylindrically blunt portion up to the cylinder/wedge junction. According to Figs. 4 and 5, it is observed that by increasing the angle of attack α causes the expected asymmetry in the heat transfer coefficient as the stagnation point moves from the symmetry axis to the cylindrically portion on the windward side of the leading edges. The stagnation region is generally considered as being the most thermally stressed zone in sharp/blunt bodies, as shown in Figs. 4 and 5. For the cases with zero-degree angle of incidence, the heat transfer coefficient at the stagnation region decreases with increasing the nose radius R_N . This behavior seems to be in agreement with the continuum predictions for blunt body in that the heat flux scales inversely with the square root of the nose radius. As expected, by reducing the nose radius R_N the leading edge becomes sharper and approaches the sharp-edged wedge, as shown in Fig. 1(a).

Before proceeding with the analysis for the other aerodynamic surface quantities, it is desirable to compare the heat flux to the body surface yielded by the simulations with that available in the literature. By analyzing experimentally the heat transfer distribution to a circular cylinder normal to a supersonic rarefied air conditions, Tewfik and Giedt (1960) proposed the following relation as an empirical fit to the experimental data,

$$\frac{q''}{q''_{\beta=0}} = 0.37 + 0.48 \cos \beta + 0.15 \cos 2\beta \quad (3)$$

where q'' is the local surface heat flux, $q''_{\beta=0}$ is the heat flux at the stagnation point, and β is the angular location along the cylinder surface measured from the stagnation point.

Since Eq. (3) was based on 20 different tests with widely differing freestream conditions and two significantly different temperature levels, Tewfik and Giedt (1960) concluded that the expression is essentially independent of the freestream conditions or wall temperature level throughout the range of their investigations. According to them, the empirical expression, defined by Eq. (3), yields a heat flux within $\pm 6\%$.

Figure 6 presents the heat transfer coefficient ratio C_h/C_{h0} to the cylindrically portion of the round leading edges as a function of the body slope angle θ for the case with zero-degree angle of incidence. In this figure, C_{h0} stands for the heat transfer coefficient at the stagnation point (Santos, 2007). For comparison purpose, the variation of the heat flux over the cylinder predicted by Eq. (3) is displayed in Fig. 6. In order to be consistent with the body slope angle θ in the present account, β in Eq. (3) corresponds to $(90-\theta)$. In addition to that, simulation prediction conducted by Carey (1994) is also presented in Fig. 6. Carey (1994) examined hot-film sensor, represented by a circular cylinder, at $M_\infty = 2.0$ and $Kn_D = 0.13$.

Referring to Fig. 6, it is seen that the heat transfer coefficient ratio obtained by the DSMC simulations for R_N/λ_∞ of 0.02 and 1.0 is in excellent agreement with the experimental data over the first 40 degrees of the leading edges, where most of the heat flux to the body surface occurs. Beyond that point, the simulations predict a slightly smaller variation. As the nose radius increases, the leading edge becomes blunt and the subsonic region between the shock wave and the round leading edges increases. In this sense, it is likely that the presence of the afterbody surface (wedge portion), which differs from a circular cylinder surface, disturbs the flowfield more upstream.

4.3. Pressure Coefficient

The pressure coefficient C_p is defined as being,

$$C_p = \frac{p_w - p_\infty}{\frac{1}{2} \rho_\infty V_\infty^2} \quad (4)$$

where p_w is the pressure acting on the body surface and p_∞ is the freestream pressure.

The pressure p_w on the body surface is calculated by the sum of the normal momentum fluxes of both incident and reflected molecules at each time step as follows,

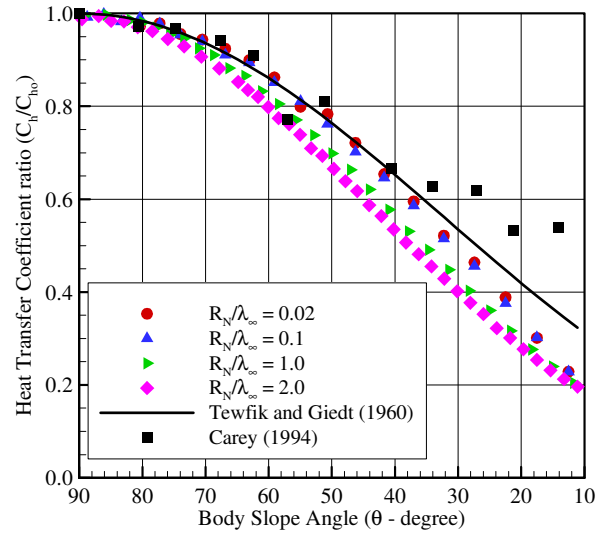


Figure 6: Distributions of heat transfer coefficient along the cylindrically portion of the leading edges as a function of the body slope angle θ .

$$p_w = p_i + p_r = \sum_{j=1}^N \left\{ m_j v_{\eta j}^2 \right\}_i + \left\{ m_j v_{\eta j}^2 \right\}_r \quad (5)$$

where v_{η} is the component of the molecular velocity normal to the body surface.

Variations of the pressure coefficient C_p , caused by changes on the angle of attack α , are demonstrated in Figs. 7 and 8 for round leading edges with R_N/λ_{∞} of 0.02 and 2.0, respectively. According to this group of figures, it is seen that the pressure coefficient follows the same trend as that presented by the heat transfer coefficient in that it presents the maximum value at the stagnation region and decreases fast in the cylindrically blunt portion of the leading edge. It is also verified that the pressure coefficient in the cylindrically blunt portion is one order of magnitude higher than the pressure coefficient in the wedge portion of the leading edges.

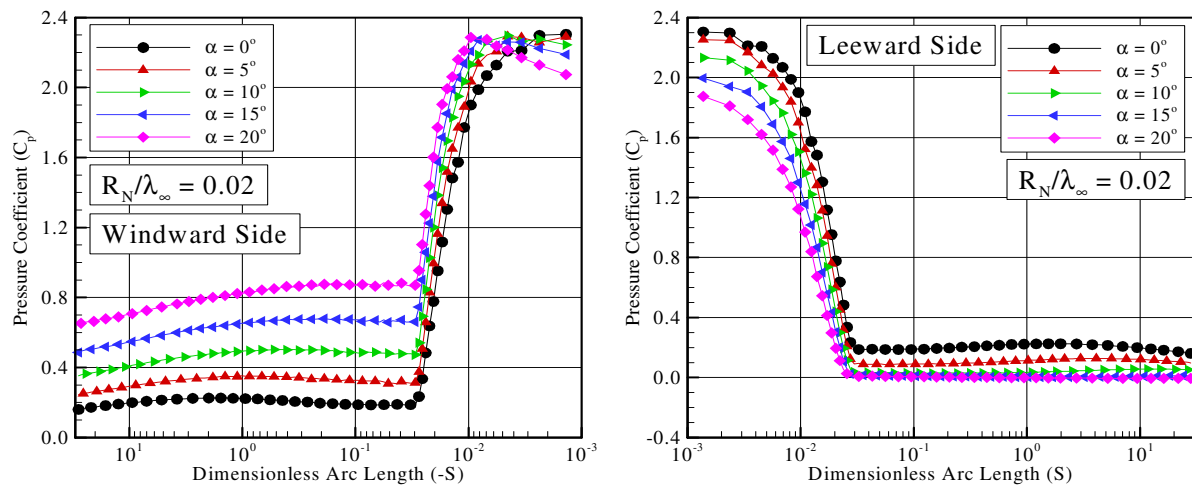


Figure 7: Distributions of pressure coefficient C_p along the (a) windward side and (b) leeward side as a function of the angle of attack for round leading edge with R_N/λ_{∞} of 0.02.

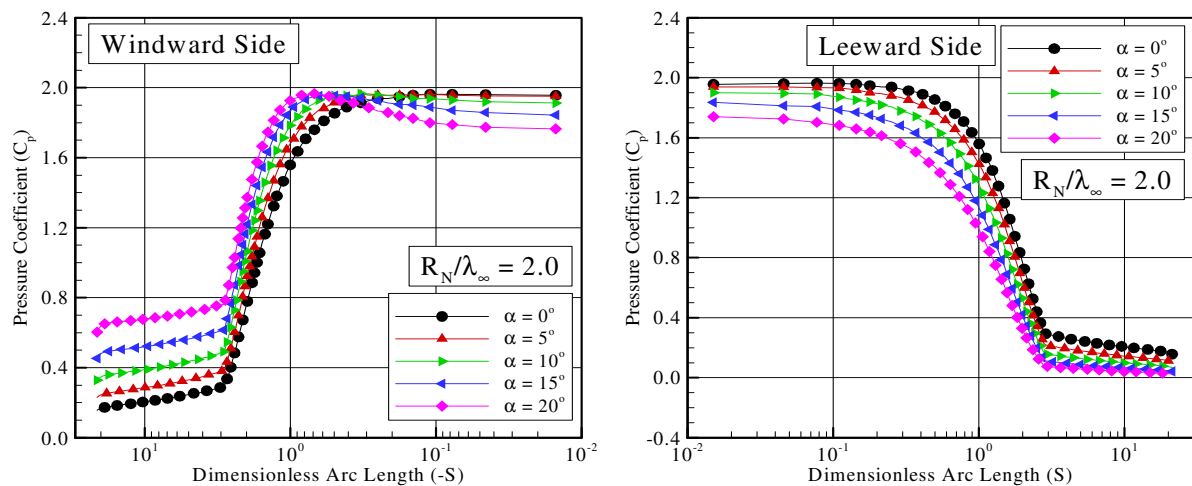


Figure 8: Distributions of pressure coefficient C_p along the (a) windward side and (b) leeward side as a function of the angle of attack for round leading edge with R_N/λ_{∞} of 2.0.

4.4. Skin Friction Coefficient

The skin friction coefficient C_f is defined as being,

$$C_f = \frac{\tau_w}{\frac{1}{2} \rho_{\infty} V_{\infty}^2} \quad (6)$$

where τ_w is the shear stress acting on the body surface.

The shear stress τ_w on the body surface is calculated by the sum of the tangential momentum fluxes of both incident and reflected molecules at each time step. Nevertheless, for the diffuse reflection model imposed for the gas-surface interaction, reflected molecules have a tangential moment equal to zero, since the molecules essentially lose, on average, their tangential velocity component. As a result, the shear stress is given by the following equation,

$$\tau_w = \tau_i + \tau_r = \sum_{j=1}^N [m_j v_{\xi_j}^2] \quad (7)$$

where v_{ξ} is the component of the molecular velocity tangent to the body surface.

The influence of the angle of attack α on the skin friction coefficient C_f is displayed in Figs. 9 and 10 for round leading edges with R_N/λ_∞ of 0.02 and 2.0, respectively. According to these plots, at zero-degree angle of incidence, the skin friction coefficient C_f is zero at the stagnation point and increases along the cylindrical portion of the leading edges up to the a maximum value around a station corresponding to 45 degrees. After that, the skin friction coefficient decreases significantly up to the cylinder/wedge junction.

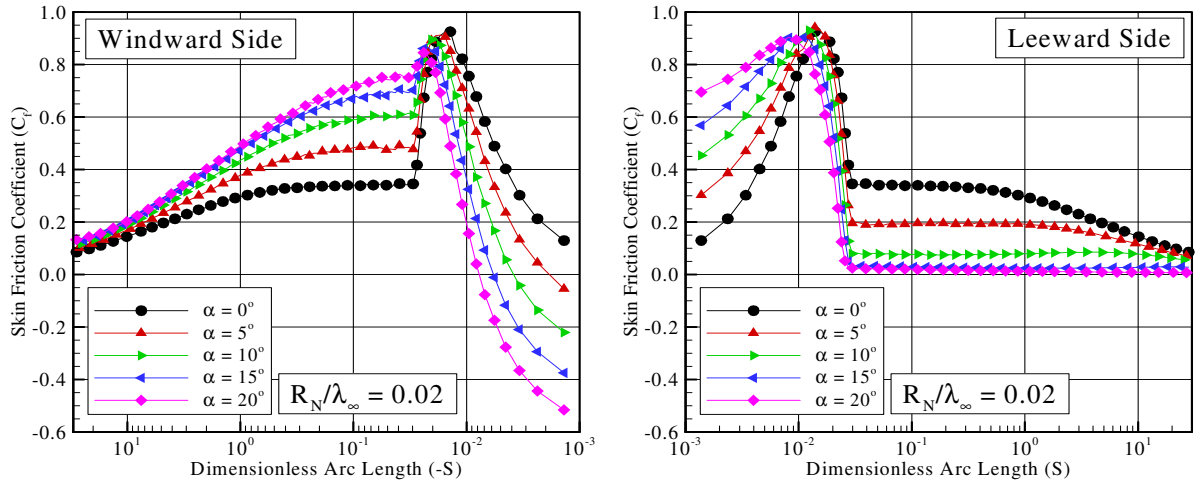


Figure 9: Distributions of skin friction coefficient C_f along the (a) windward side and (b) leeward side as a function of the angle of attack for round leading edge with R_N/λ_∞ of 0.02.

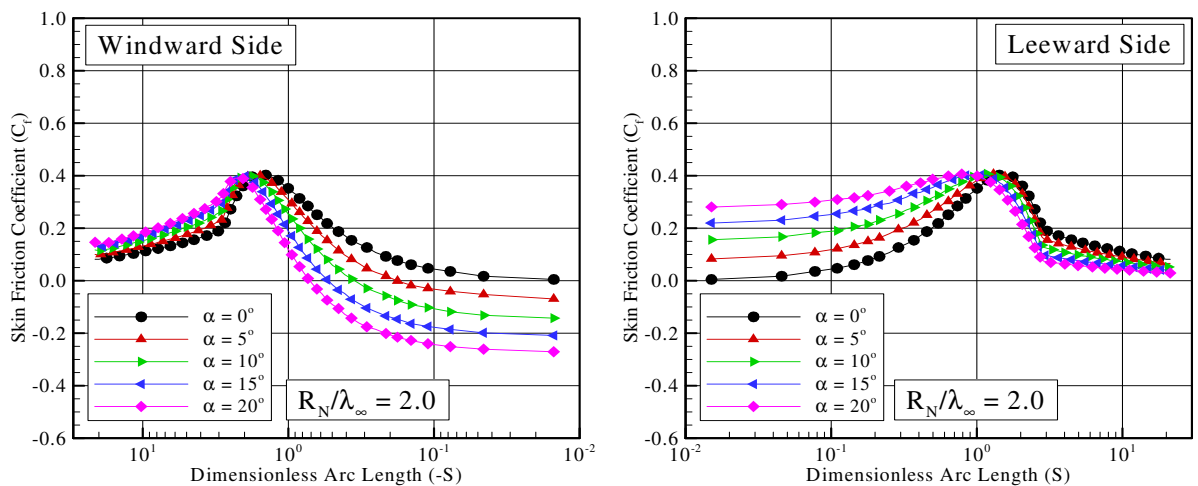


Figure 10: Distributions of skin friction coefficient C_f along the (a) windward side and (b) leeward side as a function of the angle of attack for round leading edge with R_N/λ_∞ of 2.0.

At incidence, a similar behavior is noticed for the skin friction coefficient not only on the cylindrical portion but also on the afterbody surface defined by the wedge. It is immediately evident from Figs. 9 and 10 that changes in the angle of attack α from 0 to 20 degrees produce substantial differences in the magnitude of the skin friction coefficient

along the entire body surface. It may be recognized from these plots that the skin friction coefficient C_f is essentially negative in part of the round leading edges on the windward side for angle of attack $\alpha > 0$ degree. It means that the force due to the shear stress is in the opposite direction as compared to that acting on the afterbody surface along the windward side of the body surface.

4.5. Total Drag Coefficient

The total drag coefficient C_d is defined as being,

$$C_f = \frac{F_D}{\frac{1}{2}\rho_\infty V_\infty^2 H} \quad (8)$$

where F_D is the resultant force acting on the body surface in the freestream direction and H is the height at the matching point common to the leading edges, as shown in Fig. 1(a).

The drag force on a surface in a gas flow results from the interchange of momentum between the surface and the molecules colliding with the surface. The total drag force is obtained by the integration of the pressure p_w and shear stress τ_w distributions along the windward and leeward sides in the freestream direction. This corresponds from the symmetry axis of the leading edge to the tangent point common to all the leading edges. It is noteworthy that the values for the total drag were obtained by assuming the shapes acting as leading edges. Therefore, no base pressure effects were taken into account on the calculations. Results for total drag are presented as total drag coefficient C_d and its components of pressure drag coefficient C_{pd} and the skin friction drag coefficient C_{fd} .

The angle-of-attack impact on total drag coefficient C_d is displayed in Figs. 11(a-c) for round leading edges with R_N/λ_∞ of 0.02, 1.0 and 2.0, respectively. In this group of plots, the contributions of the pressure drag C_{pd} and the skin friction drag C_{fd} to the total drag C_d are compared to those for the sharp-edged wedge shown in Fig. 1(a). In this way, filled symbols stand for the wedge and empty symbols for the round leading edges.

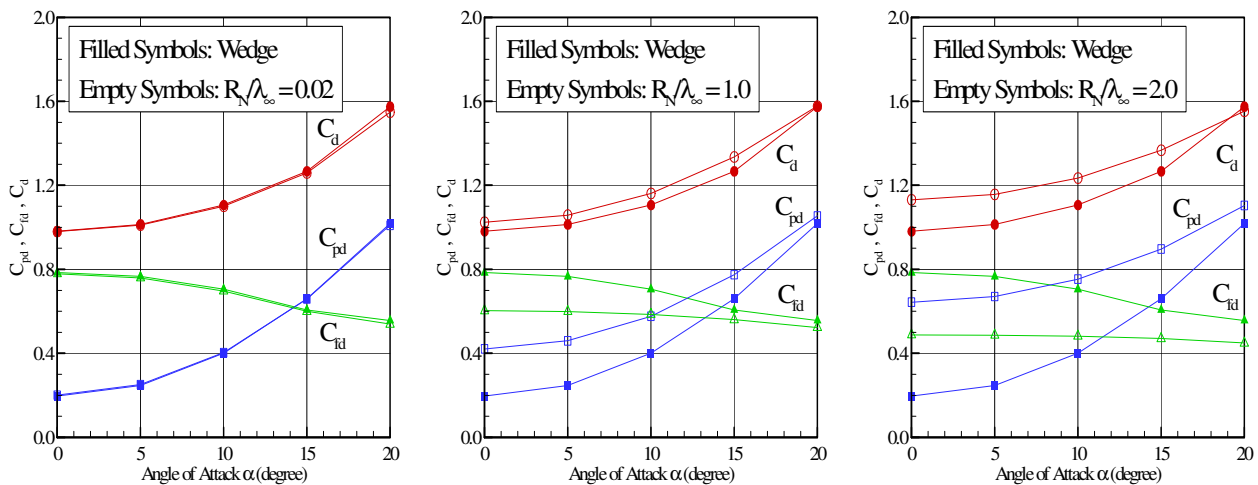


Figure 11: Pressure drag C_{pd} , skin friction drag C_{fd} and total drag C_d coefficients as a function of the angle of attack for round leading edges with R_N/λ_∞ of (a) 0.02, (b) 1.0 and (c) 2.0.

According to Figs. 11(a-c), for zero-degree angle of incidence, it is seen that as the leading edge becomes blunter, by increasing the nose radius R_N , the contribution of the pressure drag C_{pd} to the total drag increases and the contribution of the skin friction drag C_{fd} decreases. Although the net effect on total drag coefficient C_d depends on these to opposite behaviors, appreciable changes are observed in the total drag coefficient for the nose radius range investigated, since C_{pd} and C_{fd} present different rate of changes. Nevertheless, the major contribution to the total drag coefficient C_d is attributed to the skin friction coefficient C_{fd} .

Still referring to Figs. 11(a-c), it is recognized that, at incidence, the contribution of the pressure drag C_{pd} to the total drag also increases and the contribution of the skin friction drag C_{fd} decreases. The reason for that is because the leading edges become “blunt” as seen from the freestream with the angle-of-attack rise. Of particular interest is the behavior of C_{pd} and C_{fd} for angle of attack $\alpha \geq 15$ degrees. For this range of incidence, the contribution of the pressure drag C_{pd} is higher than the skin friction drag contribution C_{fd} . Also of great significance is the particular case of $\alpha = 20$ degrees. For this angle of incidence, the total drag coefficient for the sharp-edged wedge is basically the same as that presented for round leading edges.

4.6. Total Lift Coefficient

The total drag coefficient C_d is defined as being,

$$C_f = \frac{F_N}{\frac{1}{2}\rho_\infty V_\infty^2 H} \quad (9)$$

where F_N is the resultant force acting on the body surface normal to the freestream direction and H is the height at the matching point common to the leading edges (see Fig. 2(a)).

The lift force is obtained by the integration of the pressure p_w and shear stress τ_w distributions, along the windward and leeward sides, perpendicular to the freestream direction. This corresponds from the symmetry axis of the leading edge to the tangent point common to all the leading edges (see Fig. 1). Similar to the drag coefficient, results for total lift are presented as total lift coefficient C_l and its components of pressure lift coefficient C_{pl} and the skin friction lift coefficient C_{fl} .

The extent of changes on total lift coefficient C_l due to variations on the angle of attack α is illustrated in Figs. 12(a-c) for round leading edges with R_N/λ_∞ of 0.02, 1.0 and 2.0, respectively. In this set of figures, the contributions of the pressure lift C_{pl} and the skin friction lift C_{fl} to the total lift C_l are compared to those for the sharp-edged wedge.

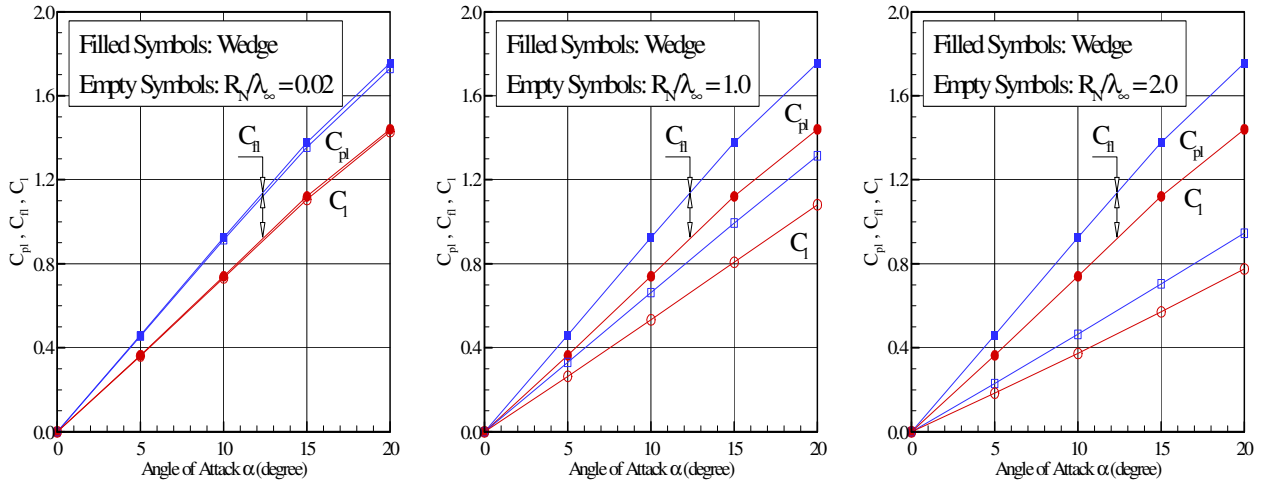


Figure 12: Pressure lift C_{pl} , skin friction lift C_{fl} and total lift C_l coefficients as a function of the angle of attack for round leading edges with R_N/λ_∞ of (a) 0.02, (b) 1.0 and (c) 2.0.

According to Figs. 12(a-c), it is noticed that the total lift C_l presents an expressive rise with increasing the angle of attack α dictated by the contribution of the pressure lift C_{pl} . In contrast, the contribution of the skin friction C_{fl} is in the sense of reducing the total lift C_l . Based on these figures, it may be inferred in passing that, as compared to the sharp-edged wedge, the total lift C_l is dramatically reduced by increasing the nose radius. It should also be mentioned in this context that, by increasing the nose radius R_N , the leading edge becomes blunt. As a result, the shock wave standoff distance increases, and the high-pressure flow from the lower surface may communicate with the flow on the upper surface, resulting in a reduction in the lift coefficient. It is usually accepted without question that the shock-wave standoff distance is directly proportional to the nose radius R_N for a circular cylinder.

4.7. Lift-to-Drag (L/D) Ratio

In order to assess the aerodynamic performance of the leading edges, the L/D ratio is presented in the following. It is known that blunt leading edges at incidence will allow leakage of the high-pressure lower surface flow into the upper surface region. As a result, lift force decreases and, consequently, causes a reduction on the L/D ratio.

The impact of the angle-of-attack on the L/D ratio is illustrated in Fig. 13 for the round leading edges investigated. For comparison purpose, the L/D ratio for the sharp-edged wedge is also presented in this figure.

According to Fig. 13, it is clearly seen that the L/D ratio increases with the angle of attack. In addition, the L/D ratio for sharp leading edges is higher than that for blunt leading edges, as would be expected. It is also seen that the L/D ratio for the sharpest round leading edge investigated, R_N/λ_∞ of 0.02, is basically the same as that found for sharp-edged wedge. As an example, for 5-degree angle of incidence, the L/D ratio for the sharp-edged wedge is 1.02, 1.44 and 2.26 times than that for round leading edges with R_N/λ_∞ of 0.1, 1.0 and 2.0, respectively. For comparison purpose, for 20-

degree angle of incidence the L/D ratio changes to 1.02, 1.33, and 1.83 times than that for round leading edges with R_N/λ_∞ of 0.1, 1.0 and 2.0, respectively.

5. CONCLUDING REMARKS

This study presented a detailed analysis of the aerodynamic surface quantities on round leading edges in rarefied hypersonic flow at incidence by employing the Direct Simulation Monte Carlo method.

Positive angle-of-attack effects on number flux, pressure, skin friction, heat transfer, drag, lift, and lift-to-drag ratio were investigated for a wide range of important parameters. The incidence ranged from 0 to 20 degrees. In addition to that, the nose radius ranged from 0.02 to 2.0 of the freestream mean free path, corresponding overall Knudsen numbers from 25 to 0.25. Cases considered in this study covered the hypersonic flow from the transitional flow regime to the free molecular flow regime.

The calculations for these round leading edges indicate that the particle simulation method predicted heat transfer about equally well as a correlation relation based on a fit to experimental data. At zero-degree angle of incidence, the peak value for the heat transfer coefficient was attained at the stagnation point. Conversely, at positive angle of incidence, the peak value for the heat transfer coefficient was attained on the windward side of the leading edges. It was found that the total drag coefficient increased by increasing the nose radius of the leading edges. Nevertheless, a significant increase in the total drag coefficient was observed by increasing the angle of attack. It was also found that the lift coefficient decreased by increasing the nose radius of the leading edge, since the leading edge changed from sharp to blunt one.

6. REFERENCES

- Bird, G. A., 1981, "Monte Carlo Simulation in an Engineering Context", Progress in Astronautics and Aeronautics: Rarefied gas Dynamics, Ed. Sam S. Fisher, Vol. 74, part I, AIAA New York, pp. 239-255.
- Bird, G. A., 1989, "Perception of Numerical Method in Rarefied Gasdynamics", Rarefied gas Dynamics: Theoretical and Computational Techniques, Eds. E. P. Muntz, and D. P. Weaver and D. H. Capbell, Vol. 118, Progress in Astronautics and Aeronautics, AIAA, New York, pp. 374-395.
- Bird, G. A., 1994, "Molecular Gas Dynamics and the Direct Simulation of Gas Flows", Oxford University Press, Oxford, England, UK.
- Borgnakke, C. and Larsen, P. S., 1975, "Statistical Collision Model for Monte Carlo Simulation of Polyatomic Gas Mixture", Journal of Computational Physics, Vol. 18, No. 4, pp. 405-420.
- Carey, V. P., 1994, "Thermal Energy Exchange between an Ultraminiature Hot-Film Sensor and a High-Speed Gas Flow", Rarefied Gas Dynamics: Experimental Technique and Physical Systems, Progress in Astronautics and Aeronautics, Eds. B. D. Shizgal and D. P. Weaver, Vol. 158, pp. 226-248.
- Nonweiler, T. R. F., 1959, "Aerodynamic Problems of Manned Space Vehicles", Journal of the Royal Aeronautical Society, Vol. 63, No. 589, pp. 521-528.
- Santos, W. F. N., 2004, "A Numerical Study of Drag and Heat Transfer to Blunt Nose Shapes in Rarefied Hypersonic Flow", Proceedings of the 24th International Congress of the Aeronautical Sciences, ICAS 2004, 29 Aug – 3 Sept, Yokohama, Japan.
- Santos, W. F. N., 2005a, "Simulation of Round Leading Edge Aerothermodynamics", Proceedings of the 18th International Congress of Mechanical Engineering COBEM 2005, 6-11 Nov, Ouro Preto, MG, Brazil.
- Santos, W. F. N., 2005b, "Aerothermodynamic Performance Comparison of Round and Flat-Nose Leading Edges at Hypersonic Flight Speed", Proceedings of the 18th International Congress of Mechanical Engineering COBEM 2005, 6-11 Nov, Ouro Preto, MG, Brazil.
- Santos, W. F. N., 2007, "Gas-Surface Interaction Effects on Round Leading Edge Aerothermodynamics". Brazilian Journal of Physics, Vol. 37, No. 2A, 337-348.
- Tewfik, O. K. and Giedt, W. H., 1960, "Heat Transfer, Recovery Factor, and Pressure Distributions Around a Circular Cylinder Normal to a Supersonic Rarefied-Air Stream", Journal of the Aerospace Sciences, Vol. 27, pp. 721-729.

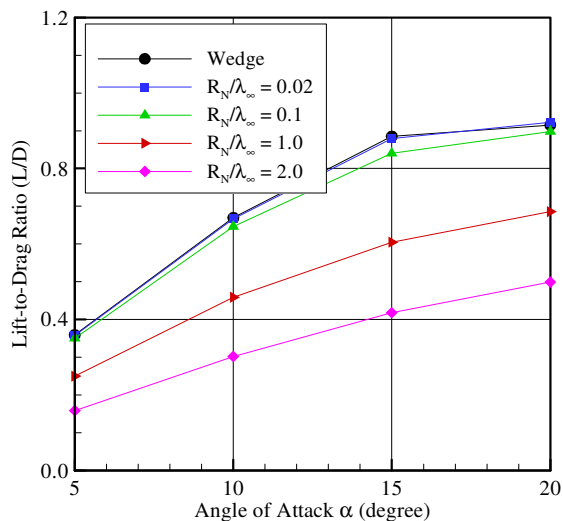


Figure 13: Comparison of the lift-to-drag ratio for round leading edge with that to sharp-edged wedge as a function of the angle of attack α .